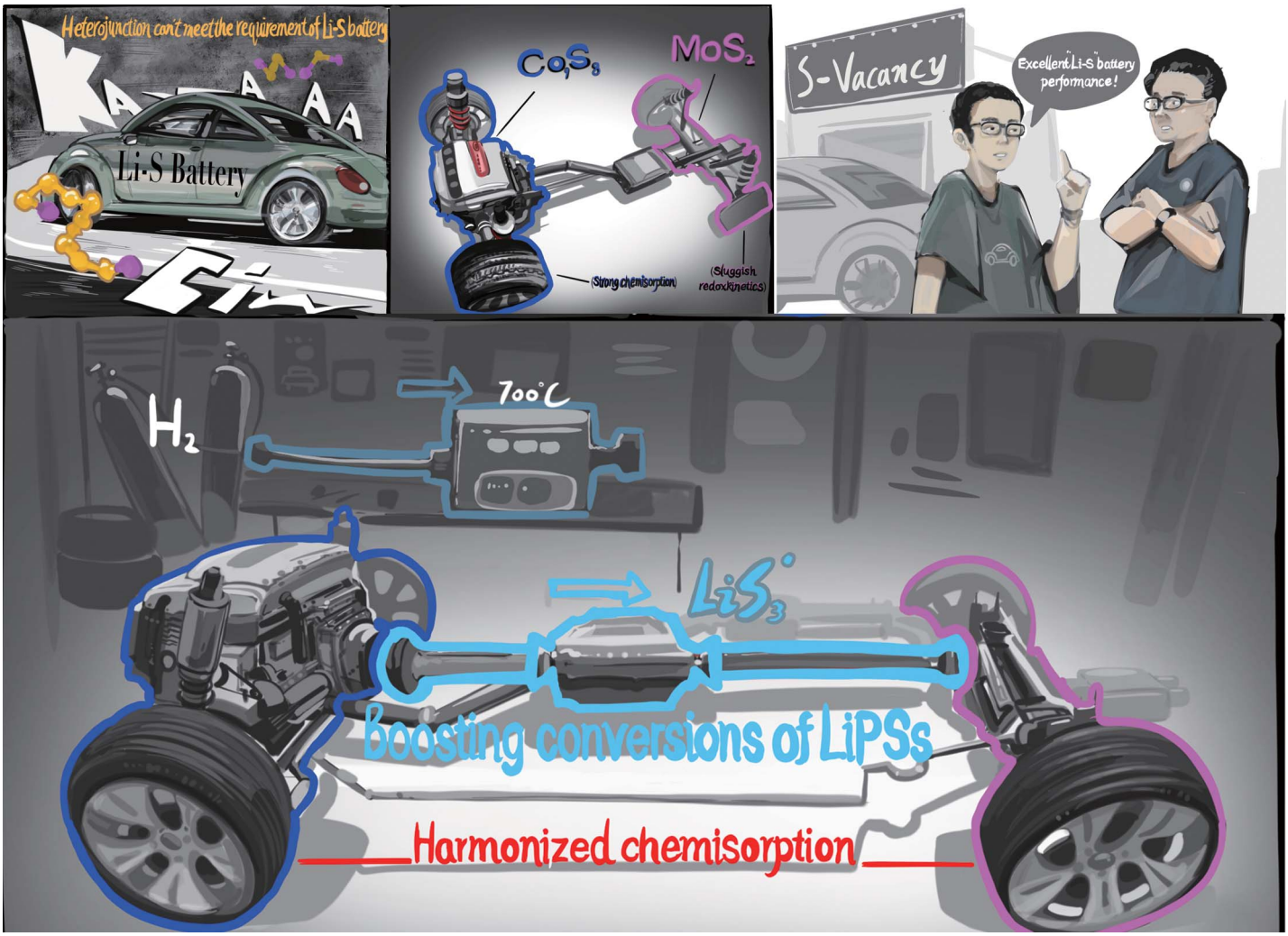

Showcasing research from Professor Zidong Wei's laboratory, School of Chemistry and Chemical Engineering, Chongqing University, Chongqing, China.

Enhanced catalysis of $LiS_3^{\cdot}$ radical-to-polysulfide interconversion *via* increased sulfur vacancies in lithium–sulfur batteries

The practical application of lithium–sulfur (Li–S) batteries is seriously hindered by severe lithium polysulfide (LiPS) shuttling and sluggish electrochemical conversions. Herein, the Co_9S_8/MoS_2 heterojunction as a model cathode host material is employed to discuss the performance improvement strategy and elucidate the catalytic mechanism. The introduction of sulfur vacancies can harmonize the chemisorption of the heterojunction component. Also, sulfur vacancies induce the generation of $LiS_3^{\cdot}$ radicals, which participate in a liquidus disproportionated reaction to reduce the accumulation of liquid LiPSs. To assess the conversion efficiency from liquid LiPSs to solid Li_2S, a new descriptor Nucleation Transformation Ratio (NTR) is proposed. NTR is defined as the ratio of the die-out amount to the formation amount of liquid LiPSs and can be calculated from basic cyclic voltammetry curves. Therefore, the transformation efficiency of S-related species in Li-S battery can be reflected quantitatively.

As featured in:

See Cunpu Li, Zidong Wei *et al.*, *Chem. Sci.*, 2022, **13**, 6224.

ROYAL SOCIETY OF CHEMISTRY

rsc.li/chemical-science

Registered charity number: 207890

Chemical Science

ROYAL SOCIETY OF CHEMISTRY

EDGE ARTICLE

View Article Online
View Journal | View Issue

Cite this: *Chem. Sci.*, 2022, **13**, 6224

All publication charges for this article have been paid for by the Royal Society of Chemistry

Received 7th March 2022
Accepted 8th May 2022

DOI: 10.1039/d2sc01353c

rsc.li/chemical-science

Enhanced catalysis of $LiS_3^{\cdot}$ radical-to-polysulfide interconversion *via* increased sulfur vacancies in lithium–sulfur batteries†

Rui Xu,‡[a] Hongan Tang,‡[a] Yuanyuan Zhou,[a] Fangzheng Wang,[a] Hongrui Wang,[a] Minhua Shao,[b] Cunpu Li *[a] and Zidong Wei *[a]

The practical application of lithium–sulfur (Li–S) batteries is seriously hindered by severe lithium polysulfide (LiPS) shuttling and sluggish electrochemical conversions. Herein, the Co_9S_8/MoS_2 heterojunction as a model cathode host material is employed to discuss the performance improvement strategy and elucidate the catalytic mechanism. The introduction of sulfur vacancies can harmonize the chemisorption of the heterojunction component. Also, sulfur vacancies induce the generation of $LiS_3^{\cdot}$ radicals, which participate in a liquidus disproportionated reaction to reduce the accumulation of liquid LiPSs. To assess the conversion efficiency from liquid LiPSs to solid Li_2S, a new descriptor calculated from basic cyclic voltammetry curves, nucleation transformation ratio, is proposed.

Introduction

With the growing demands of high-energy-storage equipment, traditional lithium-ion batteries (LIBs) could fail to meet the increasing requirements for future renewable energies. Based on the ultrahigh theoretical specific capacity (1675 mA h g^{-1}) of sulfur cathodes, lithium–sulfur (Li–S) batteries are one of the most promising and practical candidates for next-generation energy storage systems.[1–3] Nevertheless, the commercialized application of Li–S batteries is hampered by their low practical capacity and poor cyclic stability, hindering their commercialization due to the sluggish redox kinetics for lithium polysulfide (Li_2S_x, $4 \leq x \leq 8$) conversion and the notorious lithium polysulfide (LiPS) shuttling effect.[4–7] To address the above problems, designed materials are reported based on physical confinement and chemisorption. To date, many host materials have been introduced for Li–S batteries.[8–13] For example, porous carbon materials endow a porous structure to physically confine LiPS shuttling.[14] Metal oxides have excellent chemisorption to alleviate LiPS shuttling.[8,11] However, both of these strategies are passive methods to tie the LiPSs in interior or surrounding of the host materials. Driven by the concentration gradient of the soluble LiPSs, the notorious shuttling effect is still hard to avoid.[15,16] Hence, LiPSs have gained wide interest to introduce catalysis into Li–S batteries, hoping this strategy will accelerate the conversion of LiPSs for sulfur reduction reactions and sulfur evolution reactions.[17–21] Up to now, nitrides, carbides and sulfides have been widely recommended as catalysts.

From recent studies, heterojunction host materials can endow composites with favorable physicochemical properties, one component to chemisorb LiPSs and the other to catalyze LiPS conversion. Although heterojunction host materials possess certain advantages to meet the requirements of Li–S batteries, they are trapped by the limitation of finite heterointerfaces and active sites, hardly achieving the expected rapid conversion of LiPSs.[20,22] In addition, too strong chemisorption of LiPSs on one component will block soluble LiPSs from moving to the other component, where further electrochemical conversions of LiPSs take place (Scheme 1(a)). Moreover, on the liquid–solid interface, it is not easy for Li_2S_4 species to gain two electrons and convert themselves to solid-phase Li_2S_2 in the whole electrochemical conversion process.[23–26] Thus, it is difficult to obtain suitable chemisorption and accelerate the conversions of LiPSs for Li–S batteries.[15,25,27,28] Of note, defect engineering is often used to modulate the properties of materials without introducing other elements. In the case of the Co_9S_8/MoS_2 heterojunction, sulfur vacancies can be naturally thought to tailor the chemisorption and catalytic properties.[29] However, the catalytic mechanisms are usually discussed but do not expound clearly.

Based on the abovementioned discussion, reducing the accumulation of liquid LiPSs is crucial for the performance of Li–S batteries. We chose Co_9S_8/MoS_2 heterojunction composites with sulfur vacancies as a template sulfur host to demonstrate

[a]*The State Key Laboratory of Power Transmission Equipment & System Security and New Technology, Chongqing Key Laboratory of Chemical Process for Clean Energy and Resource Utilization, School of Chemistry and Chemical Engineering, Chongqing University, Shazhengjie 174, Chongqing 400044, China. E-mail: lcp@cqu.edu.cn; zdwei@cqu.edu.cn*

[b]*Department of Chemical and Biological Engineering, The Hong Kong University of Science and Technology, Clear Water Bay, Kowloon, Hong Kong*

† Electronic supplementary information (ESI) available. See https://doi.org/10.1039/d2sc01353c

‡ Rui Xu and Hongan Tang contributed equally to this paper.

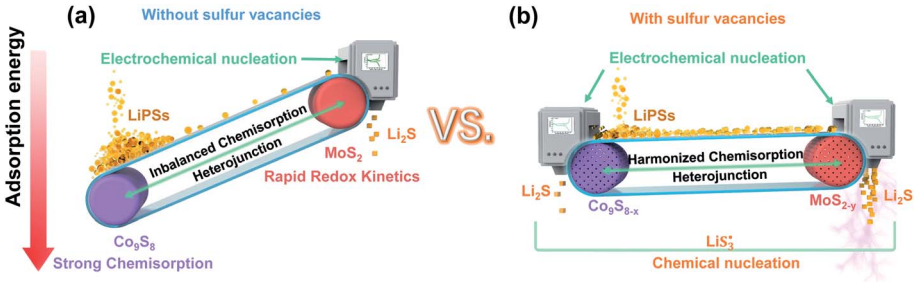

Scheme 1 Catalytic mechanism by which sulfur-vacancy heterojunctions enhance the interconversion of LiPSs. (a) Conventional Co_9S_8/MoS_2 heterojunction: Co_9S_8 was designed to adsorb liquid-phase LiPSs (orange-yellow liquid balls), while MoS_2 was used to convert LiPSs to Li_2S. However, liquid-phase LiPSs are strongly adsorbed by Co_9S_8 and therefore cannot be transferred to MoS_2 to accomplish fast conversion. (b) By the introduction of sulfur vacancies, heterojunction materials can harmonize the chemisorption of components to uniformly adsorb LiPSs and produce abundant $LiS_3^{\bullet}$ radicals to facilitate the conversion of LiPSs to Li_2S *via* a chemical nucleation route.

how sulfur vacancies modulate the behavior of the heterojunction composites with respect to chemisorption and LiPS conversions (Scheme 1(b)). With the introduction of sulfur vacancies, a large number of free radicals ($LiS_3^{\bullet}$) are generated on the sites of sulfur vacancies to promote the nucleation of Li_2S *via* a liquidus disproportionated reaction. In addition, the harmonized chemisorption of heterojunctions can speed up LiPS transport between the two components and then maximize the catalytic effect to achieve rapid LiPS conversion. Furthermore, to assess the accumulation behavior of the liquid LiPSs, a new quantitative descriptor, Nucleation Transformation Ratio (NTR), is proposed. NTR is defined as the ratio of the die-out amount to the formation amount of liquid LiPSs, and can be calculated from basic cyclic voltammetry curves. Therefore, the transformation efficiency of S-related species in Li–S battery can be reflected quantitatively.

Experimental

Chemicals

Methyl-2-pyrrolidone (NMP, 99.5 wt%), polyvinylidene fluoride (PVDF, 99.5 wt%), elemental sulfur (99.5 wt%), lithium sulfide (Li_2S, 99.98 wt%), 1,3-dioxolane (DOL, 99.8 wt%), 1,2-dimethoxyethane (DME, 99.5 wt%), tetraglyme (99 wt%), lithium bis (trifluoromethanesulfonyl) imide (LiTFSI, 99.95 wt%), lithium nitrate ($LiNO_3$, 99.99 wt%), cobalt chloride hexahydrate ($CoCl_2 \cdot 6H_2O$), potassium permanganate ($KMnO_4$, 99.5 wt%), graphite powder, ammonium tetrathiomolybdate ($(NH_4)_2MoS_4$, 99.95 wt%), reduced graphene oxide (rGO, chemically reduced) were purchased from Sigma-Aldrich. Graphene oxide (GO, >99 wt%) was purchased from Aladdin reagent. Hydrochloric acid (HCl, 37 wt%), sodium nitrate ($NaNO_3$, 99 wt%), hydrogen peroxide (H_2O_2, 30 wt%) were purchased from Chuandong Reagent. Super P carbon (99.5 wt%) from Timcal were used as received. The carbon paper (HCP120, thickness ~0.21 mm) was purchased from Shanghai HESEN Co., Ltd.

Preparation of Co_9S_8/MoS_2-rGO composite

The Co_9S_8/MoS_2-rGO composites were synthesized through a simple hydrothermal synthesis and subsequent pyrolysis process. Briefly, 100 mg of graphene oxide (GO) powder was mixed with 45 mL deionized water, then ultrasonicated for 3 h to obtain the GO suspension. $CoCl_2 \cdot 6H_2O$ (5 mL; 8 mg mL^{-1}) aqueous solution was then dropwise added into the prepared GO suspension under vigorous sonication for 30 min. Then, 35 mg $(NH_4)_2MoS_4$ dispersed in 15 mL of deionized water similarly was added into the above-mentioned suspension drop by drop. The obtained suspension was transferred into a 100 mL Teflon-lined stainless-steel autoclave. The autoclave was moved to a oven to heat at 200 °C for 24 h. After annealing to room temperature, the solid product was collected by centrifugation and then washed several times with deionized water. The precursor was then freeze–dried at −70 °C. Finally, the precursor was annealed at 700 °C in N_2 atmosphere using a heating rate of 2 °C min^{-1} to obtain the CMG-L composites.

Preparation of CMG composites

The CMG-M and CMG-H composites with sulfur deficiency were formed by heating the CMG-L products in a H_2/N_2 (10%/90%) mixed gas. The reaction temperatures were chosen for 400 °C and 700 °C. All the composites are collectively called CMG.

Preparation of sulfur composite cathode materials

The above CMG composite powders and sublimed sulfur with a weight ratio of 3 : 7 were mixed and ground. Then the mixture was heated to 155 °C and kept for 12 h in a tube furnace under an N_2 atmosphere to obtain the sulfur composite cathode materials.

Materials characterization

The prepared materials was characterized with various morphology and spectroscopy methods. The scanning electron microscopy (SEM) images were collected with a JEOL JSM-7800F. The transmission electron microscope (TEM) and high resolution transmission electron microscopy (HR-TEM) observations were performed with Tecnai G2F20 TWIN and JEM-2100F, respectively. X-ray diffraction (XRD) were performed with Rigaku D/max 2200 pc diffractometer under 40 kV and 40 mA with monochromatic Cu (K_α) radiation ($\lambda = 1.54$ Å). Raman

spectra, ultraviolet-visible (UV-Vis) spectra, and X-ray photoelectron spectroscopy (XPS) were collected with Labram HR800 (HORIBA Jobin Yvon)), Lambda 750 spectrophotometer (PerkinElmer), and ESCALAB250Xi (Thermo Scientific instrument) with Al (K_α) (1486.6 eV) radiation, respectively. Thermo gravimetric analysis (TGA) was carried out by a Mettler Toledo TGA in the temperature range of 25 to 600 °C at a heating rate of 10 °C min^{-1} under N_2 atmosphere. The pore structure and distribution was analyzed with Brunauer–Emmett–Teller (BET) method using a Micromeritics ASAP 2460 BET analyzer.

Visualized adsorption test

10 mg of rGO, CMG-L, CMG-M and CMG-H were added into 2000 μL Li_2S_6 solution with ultrasonic dispersion for 1 min, followed by static adsorption in Ar-filled glovebox. The used Li_2S_6 solution was prepared by mixing lithium sulfide and element sulfur into the electrolyte based on the mixing solvent of DOL/DME with a volume ratio of 1 : 1 to form saturated 1 mM Li_2S_6 solution. All the operations were performed in an Ar-filled glovebox. After absorption for 12 h, the supernatant solution was poured into the cuvette for UV-Vis spectrum test on a Lambda 750 spectrometer.

Li_2S nucleation tests

Elemental sulfur and Li_2S was vigorous mixed for 24 h with a molar ratio of 7 : 1 in tetraglyme to obtain the 0.20 mol L^{-1} Li_2S_8 electrolyte. Carbon papers were punched into 12 mm circle disks to load CMG composites. The loading was controlled to be 1.0 mg cm^{-2}. Lithium foils and the obtained CMG loaded carbon paper were used as the anode and cathode, respectively. LIR2032 coin cells was assembled with Celgard 2400 separator. The cathode was firstly be wetted with the previously prepared Li_2S_8 electrolyte, and the other 20 μL of LiTFSI (1.0 mol L^{-1}) was added into the LIR2032 coin cell. These cells should be firstly galvanostatically discharged to 2.06 V, and then switched to 2.05 V potentiostatically test until the current below 10^{-5} A. These procedure to guarantee the fully precipitation of Li_2S.[30]

Symmetric cell assembly and measurement

Typically, Co_9S_8/MoS_2-rGO or CMG composites were mixed with PVDF and carbon black (with a mass ratio of 3 : 1 : 1) in NMP solvent. Then the mixtures were uniformly coated onto carbon papers. The average mass loading of electrodes were controlled at about 1 mg cm^{-2}. Two identical electrodes as working and counter electrodes were assembled into a standard LIR2032 cell with a Celgard 2400 separator in an Ar-filled glovebox. 0.1 mol L^{-1} Li_2S_6 in 40.0 μL of DOL/DME (with a volume ratio of 1 : 1) was used as electrolyte, which also contained 1.0 M LiTFSI. Cyclic voltammetry (CV) tests were carried out on an electrochemical workstation (CHI660D, Shanghai Chenhua) at a scan rate of 1.0 mV s^{-1}. The voltage range of CV measurement was −0.8 to 0.8 V. The symmetric cell with Li_2S_6-free electrolyte was also tested as a reference.

Electrochemical tests

Electrochemical tests of these electrode materials were performed using coin-type (LIR2032) cells. The cells were assembled with the prepared sulfur composite cathodes (active material : carbon black : PVDF = 8 : 1 : 1), lithium anodes, electrolyte and Celgard 2400 in an argon filled glove box with extremely low H_2O and O_2 concentrations (<1.0 ppm). For compatibility of sulfur cathode and lithium anode, DOL/DME formulation which possess moderate solvating capability for LiPSs was chosen as the solvent.[31] The used electrolyte was 1 M LiTFSI dissolved in a mixed solvent of DOL/DME (volume ratio of 1 : 1). For each composite cathode, the average areal loading was around 3.2 mg cm^{-2} and sulfur content was about 68 wt%, with an electrolyte volume of 50 μL in full cells (the diameter of cathode is 12 mm, the electrolyte-to-sulfur ratio was 13.8 μL mg^{-1}). The mass of the corresponding carbon paper was measured to be around 17.7 mg. The galvanostatic charge–discharge (GCD) tests were conducted on LAND CT2001A between 1.6–2.8 V (*vs.* Li/Li^+). Galvanostatic intermittent titration technique (GITT) tests were performed on Land battery test system with discharging current of 167.2 mA g^{-1} for 0.5 h and resting for 2.5 h. The specific capacity and current rates (1C = 1672 mA h g^{-1}) were calculated on the basic of the sulfur weight in the cathode. The CV tests were performed with an electrochemical workstation CHI660D with the cut-off voltage of 1.6–2.8 V. To evaluate the conductivities of the samples, CMG samples with different sulfur vacancies were collected after annealing process. Subsequently, under the press of 10 MPa, the obtained powders (about 100 mg) were compacted *via* an infrared spectroscopy tablet mould to obtain corresponding compact sheets. It should note that the diameter of the tablet mould is 12 mm and the sheet thickness was measured with an micrometer. The obtained compact sheets were assembled in LIR2032 coin-type cells without electrolyte for conductivity tests. Electrochemical impedance spectroscopy (EIS) data were recorded by applying a sine wave with 5 mV fluctuation from a frequency range of 100 mHz to 10^3 kHz (Princeton 1260A impedance analyser). Besides, the conductivity formula is as follows:

$$R = \rho \frac{L}{S}$$

$$\sigma = \frac{1}{\rho}$$

where R is the resistance, ρ is the specific resistance, L is the thickness of sheet, S is the area of the sheet, and σ is the electronic conductivity, respectively. All the electrochemical tests were performed at room temperature.

Theoretical calculation

Vienna *ab initio* simulation package (VASP) software was used to perform the density functional theory (DFT) theoretical calculations. The DFT+U calculation was implemented with the Perdew–Burke–Ernzerhof (PBE) functional within the

generalized gradient approximation (GGA).[32,33] To assess the adsorption behavior of LiPS and base materials, a 15 Å vacuum layers was set in the *z*-direction to avoid inter-layer interactions. For all the structural optimization processes, the bottom three layers were fixed and the other atoms were fully relaxed to reach a thermodynamical stable state. The cut-off energy was set to be 500 eV. $3 \times 2 \times 1$ and $2 \times 2 \times 1$ *k*-point sampling was provided for Co_9S_8 and MoS_2, respectively. The convergence criterion was set to be 0.02 eV $Å^{-1}$ for force on each atom and 10^{-5} eV for total energies during the geometry optimization calculations. The adsorption energy (ΔE_{ads}) of the species on base surface was determined by the following equation:[33]

$$\Delta E_{ads} = E_{ads/base} - E_{ads} - E_{base}$$

where $E_{ads/base}$, E_{ads} and E_{base} are the total energy of the adsorbed systems, the isolated Li_2S_6, and base materials, respectively.

Results and discussion

From previous studies, Co_9S_8 endows strong chemisorption to alleviate LiPS shuttling.[34] In addition, MoS_2 possesses weak chemisorption yet can significantly enhance the LiPSs conversion kinetics.[35] Herein, we designed a sulfur-vacancy heterojunction material based on Co_9S_8 and MoS_2 loaded with rGO to explore the promotion mechanism. The synthetic process of CMG with different sulfur vacancy densities was prepared following a hydrothermal and annealing method in different atmospheres, as illustrated in Fig. 1(a). Consequently, we defined the obtained CMG with a low sulfur vacancy as CMG-L, a middle sulfur vacancy as CMG-M and a high sulfur vacancy as CMG-H. The characteristic peaks in XRD spectra revealed the presence of two crystal structures: MoS_2 and Co_9S_8 (Fig. S1†). XPS was used to confirm the heterojunction structure of CMG-L and MoS_2-rGO (Fig. S2†). The Mo 3d binding energy (BE) indicates that the BE peaks at 228.9 eV and 231.9 eV are pointed to Mo^{4+} for CMG-L. Compared with MoS_2-rGO, the 0.17 eV negative shift of the Mo^{4+} BE peak of CMG-L indicates the strong interaction and electron transfer between MoS_2 and Co_9S_8. This observation implies that the heterojunction structure of Co_9S_8 and MoS_2 were successfully obtained.[36,37]

Based on previous research, the annealing atmosphere and temperatures were regulated, resulting in different sulfur vacancy concentrations.[34,35,38] SEM images of the CMG composites revealed a porous, sponge-like morphology consisting of countless erect sheets with a lacunose interconnected structure (Fig. S3†). Moreover, with increasing sulfur vacancy concentration, CMG-H exhibited the largest specific surface area *via* N_2 adoption–desorption isotherms, which displayed good exposure of sulfur vacancies on the catalyst surface for LiPS interconversions (Fig. S4†).

As shown in Fig. 1(b), the XRD peaks at the same location were in good agreement with Co_9S_8 and MoS_2 for the CMG samples with different sulfur vacancy concentrations. With the increasing of the sulfur vacancy concentration, the negative shift of the 2θ degree peak at ~14° (MoS_2 (002)) and ~26° (Co_9S_8 (220)) in the expanded view (Fig. S5†) indicated lattice expansions, which were mostly caused by the removal of sulfur by hydrogen.[34,35] In addition, the XPS binding energy of Mo and Co binding energy shifted to a lower position, which also proved the partial reduction of Co_9S_8 and MoS_2 (Fig. 1(c and d)).[38] The sulfur vacancy concentrations can be calculated from the S ratio loss (from 0.09% to 0.51%) from Table S1,† which is consistent with the above analyzed fine spectra.

The sulfur-vacancy heterojunction material CMG-H was further investigated by TEM. As shown in Fig. 1(e) and S6,† the heterojunction is anchored on the reduced graphene oxide. Furthermore, Co_9S_8 exists in the form of nanoparticles, and MoS_2 exists in the form of nanosheets. HR-TEM images of the Co_9S_8/MoS_2 heterogeneous interface are shown in Fig. 1(f). Lattice fringes with spacings of 0.174 nm and 0.65 nm were indexed to the (440) plane of Co_9S_8 and the (002) plane of MoS_2, respectively. The corresponding SEAD pattern (inset of Fig. 1(f)) also consistent with both planes. Moreover, the interface between Co_9S_8 (440) and MoS_2 (002) can be observed, and discontinuous (002) and (440) facet crystal fringes also emerged on account of the presence of abundant sulfur vacancies.

It is well known that the chemisorption ability plays a significant role in inhibiting LiPS shuttling during cycling. Hence, to investigate the influence of different sulfur vacancy concentrations on chemisorption ability, first-principal calculations based on density functional theory (DFT) were used to probe the chemical adsorption energies between the components of the heterojunction and the representative soluble LiPS – Li_2S_6. As shown in Fig. 2(a), the adsorption energy between Li_2S_6 and Co_9S_8 ($\Delta E_{ads} = -3.84$ eV) is much stronger than that

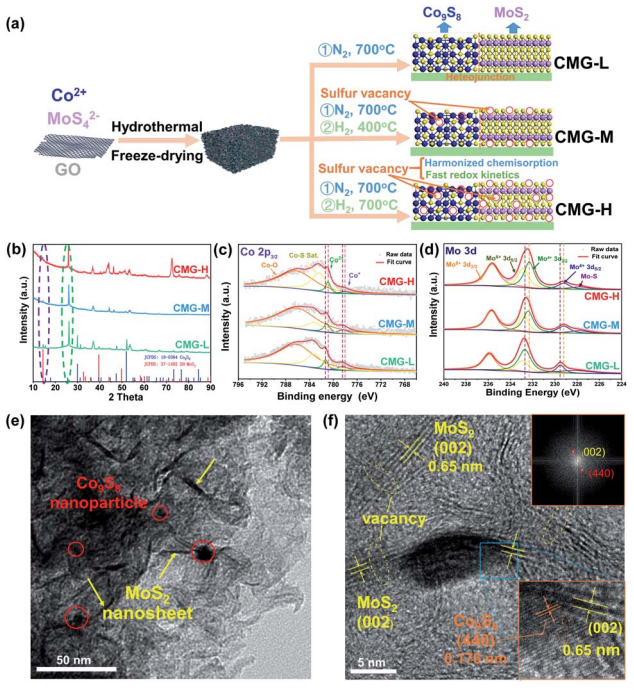

Fig. 1 (a) Schematic of the synthesis of the CMG composite; (b) XRD spectra of CMG-L, CMG-M and CMG-H; high-resolution XPS spectra of Co 2p (c) and Mo 3d (d) for CMG-L, CMG-M and CMG-H; TEM (e) and selected area electron diffraction (SAED) images (f) of CMG-H.

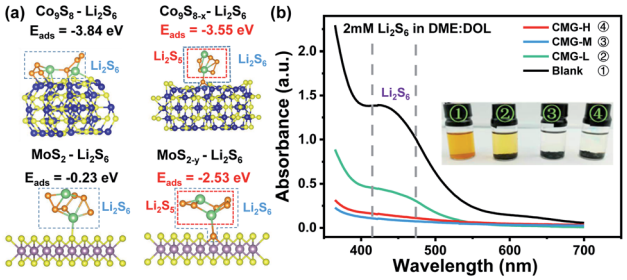

Fig. 2 (a) Calculated adsorption energies (ΔE_{ads}) of Li_2S_6 on the (002) planes of MoS_2 and MoS_{2-y} crystals as well as (220) planes of Co_9S_8 and Co_9S_{8-x} crystals; (b) the adsorption abilities of three host materials with Li_2S_6 as the representative lithium polysulfides.

between Li_2S_6 and MoS_2 ($\Delta E_{ads} = -0.23$ eV). From the view of thermodynamics, the results demonstrated that MoS_2 is relatively easily adsorbed by Li_2S_6; and Co_9S_8 is more favorable for Li_2S_6 desorption. After the introduction of sulfur vacancies, Co_9S_{8-x} presented a weaker ΔE_{ads} (−3.55 eV) than Co_9S_8 (−3.84 eV). However, the plane of MoS_{2-y} (002) showed a distinctly stronger ΔE_{ads} (−2.53 eV) than that of MoS_2 (−0.23 eV) for Li_2S_6 adsorption. In this regard, the ΔE_{ads} difference for Co_9S_{8-x} and MoS_{2-y} was significantly reduced after the introduction of sulfur vacancies. The chemisorptions strength between the heterojunction components are therefore harmonized. It is interesting that for Co_9S_{8-x} and MoS_{2-y}, one of the S atoms in the chemisorbed Li_2S_6 will be unsymmetrical adsorbed to the sulfur vacancy, then leave a relatively reactive Li_2S_5 species, which may regulate the subsequent LiPS interconversions.

The harmonized chemisorption behavior was further verified from the visualized adsorption tests. Visualized adsorption tests were adopted *via* heterojunction materials soaked in Li_2S_6 solution (inset of Fig. 2(b)). CMG-L can slightly lighten the color of the Li_2S_6 solution. The CMG-M and CMG-H composites can fully decolor the Li_2S_6 solution, suggesting their superior adsorption abilities for LiPSs. UV-Vis absorption tests provided quantitative comparisons to the chemisorption abilities of the materials. From Fig. 2(b), compared with the blank group and the CMG-L material, the CMG-M and CMG-H materials rarely showed no adsorption peaks in the 400–500 nm region for Li_2S_6.[4,39] Also, as expected from the DFT calculation, the absorbance of CMG-M material with moderate sulfur vacancies exhibited the lowest Li_2S_6 signal, which can be attributed to the harmonized chemisorption – these exists an adsorption extremum for the heterojunction materials, because the different adsorption-energy shift directions for Co_9S_{8-x} and MoS_{2-y}.

Commonly, a higher chemisorption ability corresponds to a better electrochemical performance, owing to the suppression of LiPS shuttling. However, although the chemisorption ability does not monotonously increase with sulfur vacancies, the electrochemical and battery performances nevertheless increase with sulfur vacancies. Sulfur composite cathode materials were made by the melt diffusion method (Fig. S7†) for CMG-L, CMG-M, and CMG-H. The sulfur loading was controlled to ~3.2 mg cm^{-2}, and the proportion was around 68% in the sulfur composite cathodes (Fig. S7†). Full cells were fabricated using lithium metal as the anode. From Fig. 3(a), full cells using the CMG-H electrode delivered the highest initial capacity (1129 mA h g^{-1}) and lowest capacity decay rate (0.108% per cycle, after 300 cycles) at 0.5C. Of note, the high sulfur-vacancy composite cathodes CMG-H battery delivered the best charge/discharge specific capacity (1308 mA h g^{-1}). Moreover, the plateau gap of CMG-H (190 mV) between charge/discharge is much smaller than that of CMG-L (221 mV) and CMG-M (269 mV), indicating that CMG-H possesses better kinetics during the charge/discharge process (Fig. 3(b)). In addition, as shown in Fig. 3(c), the CMG-H batteries exhibited the best rate performances, delivering discharge capacities of 1534, 1215, 1024, 938, and 816 mA h g^{-1} at rates of 0.1C, 0.2C, 0.5C, 1C, and 2C, respectively. When the rate gradually shifted back from 2C to 0.1C, the CMG-H battery also exhibited the best reversibility and excellent stability. It was extraordinary that CMG-M, with the strongest chemisorption, cannot express the best charge/discharge performance.

The electron-transport ability difference could be one contribution factor to this phenomenon. It can be found that the electronic conductivities of CMG gradually improved with the increase of sulfur vacancies, which gives rise to fast transport of electrons (Fig. S8†).[30,40] Besides, EIS measurements also registered the smallest charge transfer resistance (the size of the high-frequency semicircle in the Nyquist plot) for the CMG-H electrode (Fig. S9 and Table S2†). These results suggested that the CMG-H electrode can possess better conductivity ability, meaning that the adsorbed LiPSs can gain electrons more easily to convert to solid phase Li_2S. However, except for the conductivity difference, the reaction kinetics should also be discussed to understand the difference between CMG-M and CMG-H.

With the increase of sulfur vacancies, faster reaction kinetics could be beneficial to improve the electrochemical performance of the battery. Therefore, it is worth further to determine the reason that the slightly weaker chemisorption of the high

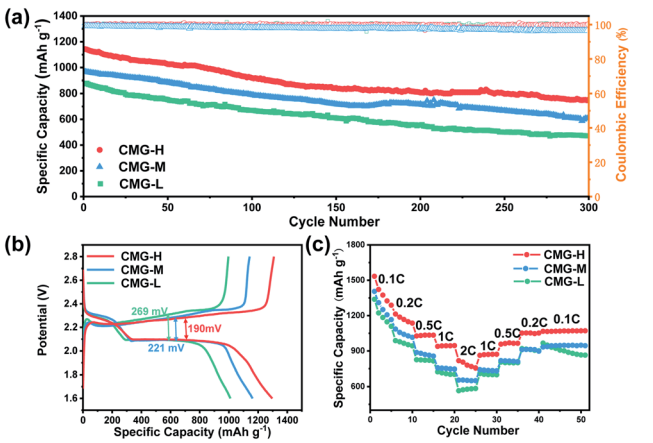

Fig. 3 (a) Long-term cycling performances of CMG-L, CMG-M and CMG-H at 0.5C. The sulfur loading was 3.2 mg cm^{-2}; (b) galvanostatic charge/discharge profiles of CMG-L, CMG-M and CMG-H at 0.2C; (c) rate capability performance of CMG-L, CMG-M and CMG-H.

sulfur-vacancy heterojunction material CMG-H exhibited better electro-chemical performance than the low sulfur-vacancy material. Hence, it is meaningful to evaluate the role of sulfur vacancies on the interconversion reactions of LiPSs. CV tests were performed within a voltage window of −0.8 V to 0.8 V for symmetrical cells assembled by heterojunction materials with different sulfur vacancies (Fig. 4(a and b)).[41] The CMG-L materials exhibited two pairs of broad peaks at −0.209/0.199 V and −0.083/0.083 V, which can be assigned to the conversion between Li_2S_6 and Li_2S_x ($x < 6$), as well as the conversion between S_8 and Li_2S_6, respectively.[42] Moreover, as the sulfur vacancies increased, the peak current densities increased and the voltage hysteresis between the cathodic peaks and anodic peaks gradually decreased, indicated that the sulfur vacancies could dynamically accelerate the electrochemical reactions of LiPSs.[43] The appearance of staged peaks at negative potentials, which correspond to the relatively short-chain polysulfide anion (S_4^{2-}) or free radical ($LiS_3^{\bullet}$), is worth comprehensively discussing to understand the role of sulfur vacancies.[18,20,34,35,39,41,44] The appearance of sulfur radicals ($LiS_3^{\bullet}$) promoted by sulfur vacancies was tested by UV-Vis spectroscopy in a 1 mM Li_2S_8 solution. Li_2S_8 solution was used to simulate the active sulfur source, and dimethyl sulfoxide (DMSO) was used as the solvent because it could stabilize $LiS_3^{\bullet}$. From Fig. 4(c), it is obvious that more sulfur vacancies correspond to more sulfur radicals ($LiS_3^{\bullet}$). Sulfur radical was believed to be generated from Li_2S_5, which was produced from the sulfur-vacancy sites and Li_2S_6 (Fig. 2(a)). The formed Li_2S_5 is extremely unstable and easily converts to other LiPS intermediates, such as $LiS_3^{\bullet}$ radicals.

It is known that $LiS_3^{\bullet}$ could accelerate the interconversion of LiPSs by providing additional chemical pathways, particularly for Li_2S deposition.[20,39,45] Therefore, to further investigate the role of sulfur vacancies, Li_2S precipitation experiments were carried out with the above three host materials as electrodes (Fig. 4(d–f)). Galvanostatic discharge was conducted to 2.06 V, and then the voltage was kept at 2.05 V until the current was below 10^{-5} A.[46] Nucleation experiments show that the capacity of precipitated Li_2S on CMG-H (254.4 mA h g_s^{-1}) is much higher than those of the two other heterojunction materials (90.6 mA h g_s^{-1} and 198.8 mA h g_s^{-1}).

As shown in the insets of Fig. 4(d–f), after the deposition of Li_2S, the surface of CMG-H is smoother and more uniform than the two other materials. It is interesting that the Li_2S peak appeared much earlier for CMG-H than the others during the galvanostatic discharge process. This observation implies that the reduction reactions of LiPSs to Li_2S occur much easier in CMG-H cathode, which can contribute to the detected electric current earlier. We named this current generated from all the S-related species involved reactions as the hybrid current. The earlier occurrence of the Li_2S deposition current suggests that the liquid LiPSs will not accumulate but fastly be reduced to solid Li_2S. Therefore, in the hybrid current, a greater

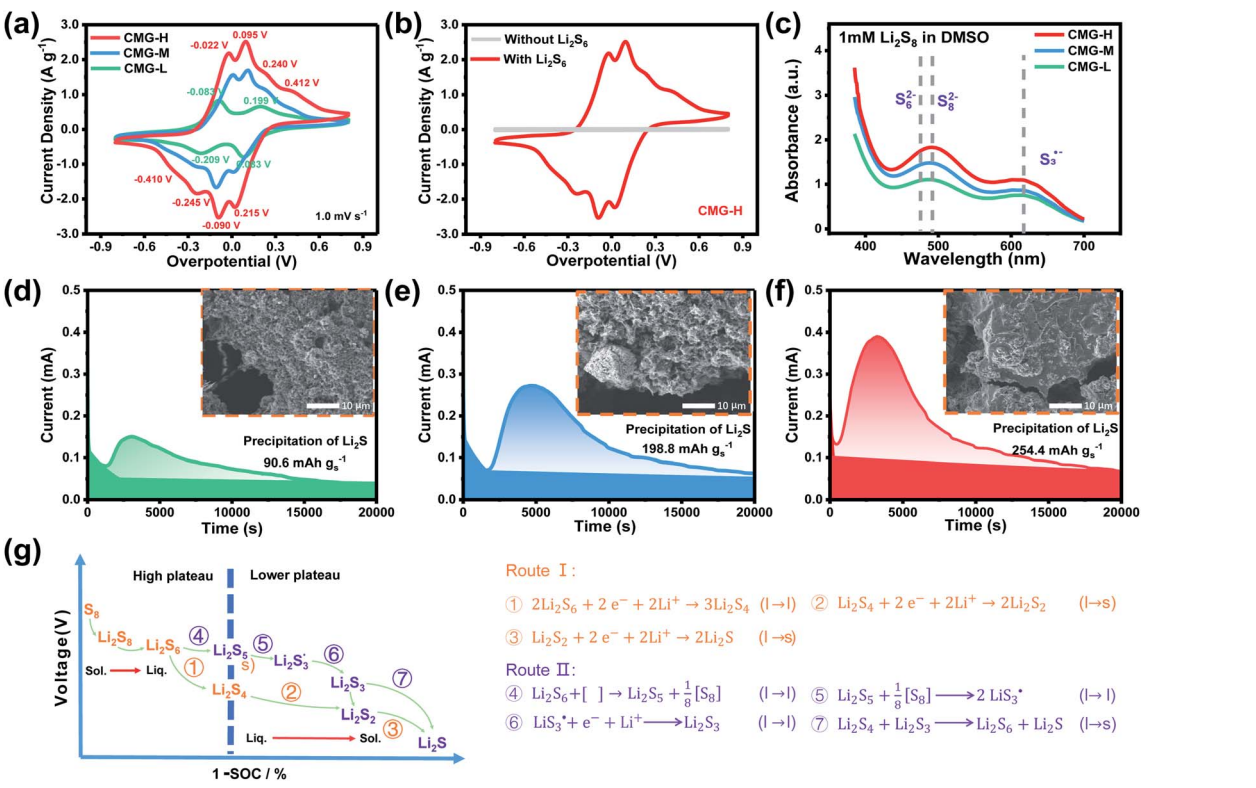

Fig. 4 (a) Cyclic voltammograms of symmetric cells at 1 mV s^{-1}; (b) cyclic voltammograms of symmetric cells with and without Li_2S_6 solution; (c) the variation in UV absorbance with increasing sulfur vacancy concentration (d–f) potentiostatic discharging curves of Li_2S_8/tetraglyme solution at 2.05 V and the corresponding SEM images after Li_2S deposition; (g) proposed sulfur reduction reaction routes for the Li–S battery with the sulfur-vacancy heterojunction material.

contribution from LiPSs conversion to Li_2S will decrease LiPSs shuttling to increase the stability of Li–S battery.

Based on the above discussion of the relationship of chemisorption and sulfur vacancies, the sulfur vacancies in the heterojunction could not only to harmonize the chemisorption, but also to adjust the redox kinetics process of LiPSs as follows. As illustrated in Fig. 4(g), harmonization of the chemisorption could hold back the LiPS shuttling. In the meantime, without the participation of $LiS_3^{\bullet}$, only the conventional electrochemical nucleation route (route I) can accomplish liquid–solid transformation. As the electrochemical requirement is crucial for liquid-phase Li_2S_4 to gain two electrons on the liquid–solid interface of the cathode to be converted to solid-phase Li_2S_2.[43,47] Li_2S and Li_2S_2 deposition is controlled by the sparsely distributed nucleation sites on the liquid–solid interface of the cathode. In comparison, in addition to the route I, sulfur vacancies can promote the formation of sulfur radicals ($LiS_3^{\bullet}$) to accelerate liquid-phase conversion (chemical nucleation route, route II). Taking the discharge process as an example, sulfur vacancies chemisorb Li_2S_6 to form reactive Li_2S_5, and then Li_2S_5 reacts with solid S_8 to form $LiS_3^{\bullet}$.[47–50] Liquid-phase $LiS_3^{\bullet}$ gains one electron and one Li^+ to convert to liquidus Li_2S_3 (reaction ⑦). Then, Li_2S_3 may react with Li_2S_4 to convert to Li_2S_6 and solid-phase Li_2S *via* a spontaneous liquid-phase disproportionated reaction ($\Delta H = -1.31$ eV), simultaneously achieving the formation of homogeneous nucleation sites.

As the function of $LiS_3^{\bullet}$ is crucial for the deposition of Li_2S and the formation of the hybrid current, the redox kinetics of heterojunctions with different sulfur vacancies were further studied by CV (Fig. 5(a–c)).[51] Two cathodic peaks, located at 2.20–2.30 V (peak 1) and 1.80–2.05 V (peak 2) should correspond to the reduction of sulfur into high-order LiPSs (Li_2S_x, $4 \le x \le 8$) and further LiPSs to low-order Li_2S_2/Li_2S.[24–26,52] Simultaneously, the broad anodic peaks should be assigned to the oxidation of Li_2S_2/Li_2S to Li_2S_6/S_8 *via* the formation of intermediate LiPSs.[53] Compared with the CMG-L and CMG-M electrodes, the CMG-H electrode showed distinguished, smaller polarization, demonstrating that peak 1 and peak 2 of CMG-H shifted 0.03 V and 0.07 V, respectively, with the scan rate increase (Fig. 5(a–c)).

High-efficiency Li_2S deposition was quantitatively analysed *via* CV curves. The discharge currents for peak 1 and peak 2 were integrated with time as the quantities of charge for the corresponding reactions. Herein, the quantity of electron transfer was defined for the three heterojunctions based on the following equation:

$$C_e = \frac{A_t}{v} \quad (1)$$

where C_e is the amount of electron transfer per gram (A s), A_t is the integral area (A V) of peak 1 and peak 2, and v is the scan rate (V s^{-1}). In addition to the above discussed polarization behaviors, the calculated C_e can provide quantitative information for the interconversions of the LiPSs.

As illustrated in Table 1, 1 mol of solid-phase S_8 molecules will obtain 4 mol of electrons to form 2 mol of liquid-phase Li_2S_4, which corresponds to peak 1 (reaction (1) in Table 1). These Li_2S_4 molecules will gain 12 mol of electrons to yield 8 mol of Li_2S (peak 2, reaction (2) in Table 1). Therefore, a quantitative descriptor, named as Nucleation Transformation Ratio (NTR), to assess the kinetics behaviors of the cathode reactions can be defined:

$$\mathrm{NTR} = \frac{C_{e2}}{C_{e1}} \quad (2)$$

where C_{e1} and C_{e2} are the calculated C_es for peak 1 and peak 2, respectively. NTR can reflect the ratio of the reacted Li_2S_4 in peak 2 (die-out amount of LiPSs) to the produced Li_2S_4 in peak 1 (formation amount of LiPSs, more details in Fig. S10†). Based on the discussions in Table 1, the ideal NTR should be 3. The

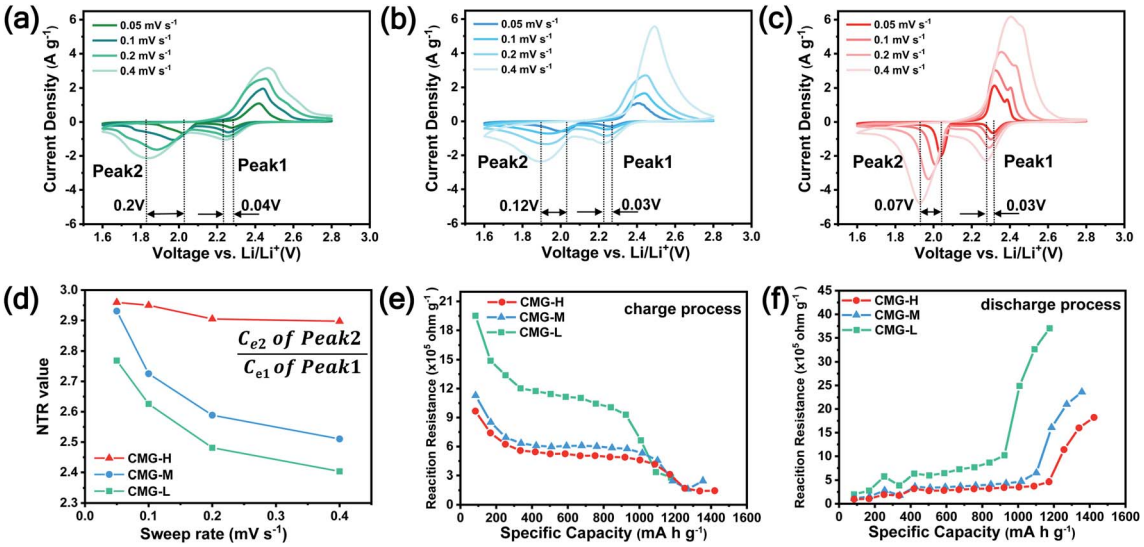

Fig. 5 CV curves within the voltage range of 1.6–2.8 V at different sweep rates: (a) CMG-L. (b) CMG-M. (c) CMG-H. (d) The NTR values of CMG-L, CMG-M and CMG-H at different sweep rates; *in situ* reaction resistances during discharge (e) and charge (f) processes of CMG-L, CMG-M and CMG-H during GITT measurement.

Table 1 The reaction equation and electron-transfer number of Li–S batteries

Peak	Reaction	Phase	Electron transfer number	Reaction
1	$S_8 + 4e^- + 4Li^+ \rightarrow 2Li_2S_4$	Solid → liquid	4	(1)
2	$2Li_2S_4 + 12e^- + 12Li^+ \rightarrow 8Li_2S$	Solid → liquid	12	(2)

calculated NTR is closer to 3, the closer the conversion of Li_2S_4 to Li_2S is to the ideal conditions. All the NTR values for CMG composites at different scan rates were calculated and are illustrated in Fig. 5(d) and Table S3.† At a lower scan rate (0.05 mV s^{-1}), all the NTR values for the three samples were close to 3, while CMG-H exhibited the largest NTR = 2.96. As the scan rate increased, the voltage rapidly passed through the reactive window. Under high scan rate conditions, the produced Li_2S_4 from peak 1 cannot rapidly be converted to Li_2S (peak 2) when the Li_2S nucleation is blunt. As shown in Fig. 5(d), although the NTR for CMG-L and CMG-M decreased rapidly (2.40 for CMG-L and 2.51 for CMG-M at 0.4 mV s^{-1}, respectively), the NTR for CMG-H remains close to 3. Meanwhile, the CMG-H electrodes exhibited an obvious bigger integral area compared with others, which implies that CMG-H can release more current under same potential. This is the reason why the CMG-H, which do not possess the strongest LiPSs chemisorption ability, can exhibit the best Li–S cell performance. Moreover, these results indicate that the liquid–solid conversions for LiPSs to Li_2S can be readily performed in CMG-H, which should be attributed to the abundant generated LiS_3^*, followed by the disproportionated nucleation reaction. The fastest Li^+ ion diffusion also confirmed the rapid conversion *via* the Randles–Sevcik equation, which validated our introduced NTR in the peak current vision (see further Discussion in ESI and Fig. S11 and S12†). In addition, the GITT measurements were performed. A constant current density of 167.2 mA g^{-1} (the theoretical 0.1C current for 1 g of sulfur) was applied for 1 h, and a pulse duration of 2.5 h was applied to collect the potential response after the first active cycle, as presented in Fig. 5(e), (f) and S13.†[54] CMG-H consistently expressed the lowest reaction resistances in both charge/discharge processes, suggesting a minimum LiPS interconversion barrier.

Conclusions

In summary, we introduced sulfur vacancies into heterojunction materials and conducted a systematic investigation of the chemisorption and kinetics of heterojunctions with increasing sulfur vacancies in Li–S cells. Chemisorption can be harmonized to realize a uniform distribution of LiPSs in the heterojunction. The introduction of sulfur vacancies can generate a large amount of LiS_3^* radicals, which can promote the nucleation of Li_2S *via* a spontaneous disproportionated reaction. The formation of Li_2S can participate in the hybrid current in the early discharge stage to reduce the accumulation of liquid LiPSs. Additionally, the defined descriptor nucleation transformation ratio was applied to quantitatively elucidate the kinetic behaviors of the materials and understand Li–S full battery performance. The catalytic mechanisms were therefore elucidated and paved the way for material design and theoretical direction.

Author contributions

C. L. and Z. W. directed the project. H. Tang and R. Xu performed the main experimental works. Y. Z., F. W. and H. W. participate in some of experimental works. R. X. analysed the data and wrote the manuscript. R. X. and H. T. contributed equally. All the authors discussed the results.

Conflicts of interest

There are no conflicts to declare.

Acknowledgements

This research work was financially sponsored by National Natural Science Foundation of China (Grant No: 22075033, U21A20312, and 91834301).

Notes and references

1 R. Gan, N. Yang, Q. Dong, N. Fu, R. Wu, C. Li, Q. Liao, J. Li and Z. Wei, *J. Mater. Chem. A*, 2020, **8**, 7253–7260.
2 Q. Dong, R. Shen, C. Li, R. Gan, X. Ma, J. Wang, J. Li and Z. Wei, *Small*, 2018, **14**, 1804277.
3 P. G. Bruce, S. A. Freunberger, L. J. Hardwick and J.-M. Tarascon, *Nat. Mater.*, 2012, **11**, 19–29.
4 W. Chen, T. Lei, W. Lv, Y. Hu, Y. Yan, Y. Jiao, W. He, Z. Li, C. Yan and J. Xiong, *Adv. Mater.*, 2018, **30**, 1804084.
5 Z. Cheng, H. Pan, J. Chen, X. Meng and R. Wang, *Adv. Energy Mater.*, 2019, **9**, 1901609.
6 Q. Dong, T. Wang, R. Gan, N. Fu, C. Li and Z. Wei, *ACS Appl. Mater. Interfaces*, 2020, **12**, 20596–20604.
7 X. Ji, K. T. Lee and L. F. Nazar, *Nat. Mater.*, 2009, **8**, 500–506.
8 E. H. M. Salhabi, J. Zhao, J. Wang, M. Yang, B. Wang and D. Wang, *Angew. Chem.*, 2019, **131**, 9176–9180.
9 D.-R. Deng, F. Xue, Y.-J. Jia, J.-C. Ye, C.-D. Bai, M.-S. Zheng and Q.-F. Dong, *ACS Nano*, 2017, **11**, 6031–6039.
10 Z. Sun, J. Zhang, L. Yin, G. Hu, R. Fang, H.-M. Cheng and F. Li, *Nat. Commun.*, 2017, **8**, 1–8.
11 Z. Li, J. Zhang and X. W. Lou, *Angew. Chem.*, 2015, **127**, 13078–13082.
12 Z. Yuan, H.-J. Peng, T.-Z. Hou, J.-Q. Huang, C.-M. Chen, D.-W. Wang, X.-B. Cheng, F. Wei and Q. Zhang, *Nano Lett.*, 2016, **16**, 519–527.

13 F. Zhou, Z. Li, X. Luo, T. Wu, B. Jiang, L.-L. Lu, H.-B. Yao, M. Antonietti and S.-H. Yu, *Nano Lett.*, 2018, **18**, 1035–1043.
14 H. Pan, Z. Cheng, Z. Xiao, X. Li and R. Wang, *Adv. Funct. Mater.*, 2017, **27**, 1703936.
15 L. Peng, Z. Wei, C. Wan, J. Li, Z. Chen, D. Zhu, D. Baumann, H. Liu, C. S. Allen, X. Xu, *et al.*, *Nat. Catal.*, 2020, **3**, 762–770.
16 X. Ding, S. Yang, S. Zhou, Y. Zhan, Y. Lai, X. Zhou, X. Xu, H. Nie, S. Huang and Z. Yang, *Adv. Funct. Mater.*, 2020, **30**, 2003354.
17 T. Zhou, W. Lv, J. Li, G. Zhou, Y. Zhao, S. Fan, B. Liu, B. Li, F. Kang and Q.-H. Yang, *Energy Environ. Sci.*, 2017, **10**, 1694–1703.
18 Y. Song, W. Zhao, L. Kong, L. Zhang, X. Zhu, Y. Shao, F. Ding, Q. Zhang, J. Sun and Z. Liu, *Energy Environ. Sci.*, 2018, **11**, 2620–2630.
19 L. Zhang, Y. Liu, Z. Zhao, P. Jiang, T. Zhang, M. Li, S. Pan, T. Tang, T. Wu, P. Liu, *et al.*, *ACS Nano*, 2020, **14**, 8495–8507.
20 M. Zhang, W. Chen, L. Xue, Y. Jiao, T. Lei, J. Chu, J. Huang, C. Gong, C. Yan, Y. Yan, *et al.*, *Adv. Energy Mater.*, 2020, **10**, 1903008.
21 H. Ye, J. Sun, S. Zhang, H. Lin, T. Zhang, Q. Yao and J. Y. Lee, *ACS Nano*, 2019, **13**, 14208–14216.
22 X. Liu, J.-Q. Huang, Q. Zhang and L. Mai, *Adv. Mater*, 2017, **29**, 1601759.
23 Z. Liu, P. B. Balbuena and P. P. Mukherjee, *J. Phys. Chem. Lett.*, 2017, **8**, 1324–1330.
24 C.-S. Cheng and S.-H. Chung, *Chem. Eng. J.*, 2022, **429**, 132257.
25 Y.-J. Yen and S.-H. Chung, *ACS Appl. Mater. Interfaces*, 2021, **13**, 58712–58722.
26 C. Geng, W. Hua, D. Wang, G. Ling, C. Zhang and Q.-H. Yang, *SusMat*, 2021, **1**, 51–65.
27 Y. Wei, B. Wang, Y. Zhang, M. Zhang, Q. Wang, Y. Zhang and H. Wu, *Adv. Funct. Mater.*, 2021, **31**, 2006033.
28 C. Zu, L. Li, J. Guo, S. Wang, D. Fan and A. Manthiram, *J. Phys. Chem. Lett.*, 2016, **7**, 1392–1399.
29 J. Qian, S. Wang, Y. Li, M. Zhang, F. Wang, Y. Zhao, Q. Sun, L. Li, F. Wu and R. Chen, *Adv. Funct. Mater.*, 2021, **31**, 2006950.
30 Y. Zhang, P. Chen, Q. Wang, Q. Wang, K. Zhu, K. Ye, G. Wang, D. Cao, J. Yan and Q. Zhang, *Adv. Energy Mater.*, 2021, **11**, 2101712.
31 Y. Liu, Y. Elias, J. Meng, D. Aurbach, R. Zou, D. Xia and Q. Pang, *Joule*, 2021, **5**, 2323–2364.
32 M. Bajdich, M. García-Mota, A. Vojvodic, J. K. Nørskov and A. T. Bell, *J. Am. Chem. Soc.*, 2013, **135**, 13521–13530.
33 C. Huang, Z.-Q. Wang and X.-Q. Gong, *Chin. J. Catal.*, 2018, **39**, 1520–1526.
34 H. Lin, S. Zhang, T. Zhang, S. Cao, H. Ye, Q. Yao, G. W. Zheng and J. Y. Lee, *ACS Nano*, 2019, **13**, 7073–7082.
35 H. Lin, L. Yang, X. Jiang, G. Li, T. Zhang, Q. Yao, G. W. Zheng and J. Y. Lee, *Energy Environ. Sci.*, 2017, **10**, 1476–1486.
36 L. Diao, B. Zhang, Q. Sun, N. Wang, N. Zhao, C. Shi, E. Liu and C. He, *Nanoscale*, 2019, **11**, 21479–21486.
37 J. Ru, T. He, B. Chen, Y. Feng, L. Zu, Z. Wang, Q. Zhang, T. Hao, R. Meng, R. Che, *et al.*, *Angew. Chem.*, 2020, **132**, 14729–14735.
38 W.-G. Lim, C. Jo, A. Cho, J. Hwang, S. Kim, J. W. Han and J. Lee, *Adv. Mater.*, 2019, **31**, 1806547.
39 Q. Zou and Y.-C. Lu, *J. Phys. Chem. Lett.*, 2016, **7**, 1518–1525.
40 X. Zhang, Q. Liao, Z. Kang, B. Liu, X. Liu, Y. Ou, J. Xiao, J. Du, Y. Liu, L. Gao, *et al.*, *Adv. Mater.*, 2021, **33**, 2007051.
41 R. Li, H. Peng, Q. Wu, X. Zhou, J. He, H. Shen, M. Yang and C. Li, *Angew. Chem., Int. Ed.*, 2020, **59**, 12129–12138.
42 S. Rehman, T. Tang, Z. Ali, X. Huang and Y. Hou, *Small*, 2017, **13**, 1700087.
43 Z. Du, X. Chen, W. Hu, C. Chuang, S. Xie, A. Hu, W. Yan, X. Kong, X. Wu, H. Ji, *et al.*, *J. Am. Chem. Soc.*, 2019, **141**, 3977–3985.
44 H. Lin, S. Zhang, T. Zhang, H. Ye, Q. Yao, G. W. Zheng and J. Y. Lee, *Adv. Energy Mater.*, 2018, **8**, 1801868.
45 M. Cuisinier, C. Hart, M. Balasubramanian, A. Garsuch and L. F. Nazar, *Adv. Energy Mater.*, 2015, **5**, 1401801.
46 F. Y. Fan, W. C. Carter and Y.-M. Chiang, *Adv. Mater*, 2015, **27**, 5203–5209.
47 P. Schön, F. Hintz and U. Krewer, *Electrochim. Acta*, 2019, **295**, 926–933.
48 K. H. Wujcik, T. A. Pascal, C. Pemmaraju, D. Devaux, W. C. Stolte, N. P. Balsara and D. Prendergast, *Adv. Energy Mater.*, 2015, **5**, 1500285.
49 Q. Wang, J. Zheng, E. Walter, H. Pan, D. Lv, P. Zuo, H. Chen, Z. D. Deng, B. Y. Liaw, X. Yu, *et al.*, *J. Electrochem. Soc.*, 2015, **162**, A474.
50 A. Kumar, A. Ghosh, M. Forsyth, D. R. MacFarlane and S. Mitra, *ACS Energy Lett.*, 2020, **5**, 2112–2121.
51 J.-P. Jones, S. C. Jones, F. C. Krause, J. Pasalic and R. Bugga, *J. Phys. Chem. Lett.*, 2018, **9**, 3751–3755.
52 X. Gao, X. Yang, M. Li, Q. Sun, J. Liang, J. Luo, J. Wang, W. Li, J. Liang, Y. Liu, *et al.*, *Adv. Funct. Mater.*, 2019, **29**, 1806724.
53 B. Li, Q. Su, L. Yu, J. Zhang, G. Du, D. Wang, D. Han, M. Zhang, S. Ding and B. Xu, *ACS Nano*, 2020, **14**, 17285–17294.
54 G. Liu, C. Yuan, P. Zeng, C. Cheng, T. Yan, K. Dai, J. Mao and L. Zhang, *J. Energy Chem.*, 2022, **67**, 73–81.